ERC | CISST

JOHNS HOPKINS UNIVERSITY

Guidance for Skull Base Surgery

Team 10: Allen Zhu, Grace Yeo

Mentors: Dr. Peter Kazanzides, Dr. Muyinatu Bell

Abstract

Transsphenoidal skull base surgery gives access to the pituitary region through the sphenoid sinus and is the preferred method of entry in adults. However, it is technically more difficult in children due to their smaller anatomy, and the region includes critical structures such as the carotid artery on either side of the sinus that must be avoided. Current computer-integrated appraoches to skull base surgeries are unable to consistently achieve errors below the clinical threshold. To this end, we developed a software framework that incorporates intra-operative simulated photo-acoustic ultrasound. We were able to show that simulated intraoperative photo-acoustic imaging is able to reduce error to below clinical error values of 1mm, thereby improving the feasiblity of this modified system for clinical use.

1. Introduction

1.1 Motivation and Relevance

1.1.1 Skull Base Surgery and the Transphenoidal Approach

In skull base surgery, the transsphenoidal approach is the preferred method of entry for removal of tumors in the pituitary region. During this surgery, a small portion of the nasal septum is removed so that a drill can be inserted through the nose to gain access to the sphenoid sinus.

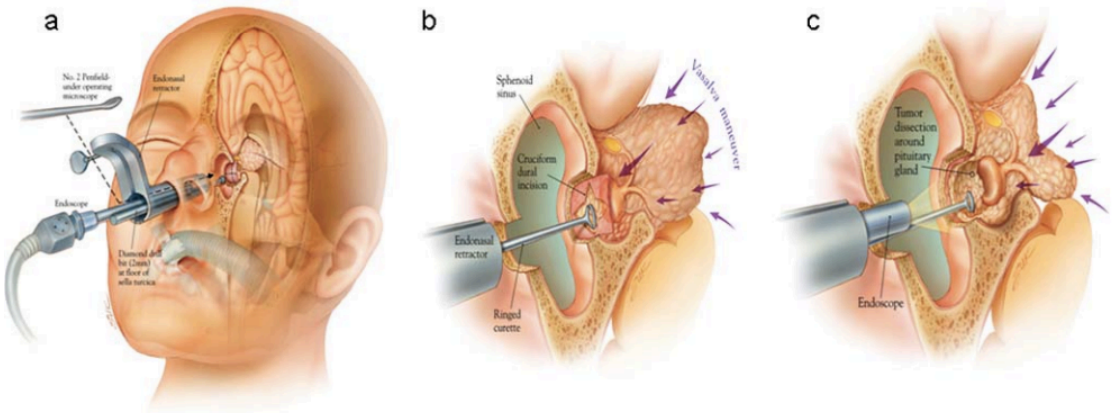

Figure 1: The transphenoidal approach for the removal of tumors in the pituitary region. Image source: JF Frazier, K Chaichana, GI Jallo, A Quiñones-Hinojosa, "Combined endoscopic and microscopic management of pediatric pituitary region tumors through one nostril: technical note with case illustrations", *Childs Nervous System*, Vol 24, pp 1469–1478, 2008

The front wall of the sphenoid sinus is drilled through, granting access to the actual sinus. The back wall of the sinus, called the sella, lies directly over the pituitary gland. It is also drilled through and this gives access to the tumor. This surgery is technically challenging in children because of their smaller anatomy and unaerated sinuses. These make it much harder to avoid critical structures such as the carotid artery, which lies on the sides of the sinus, while drilling (Frazier, 2008).

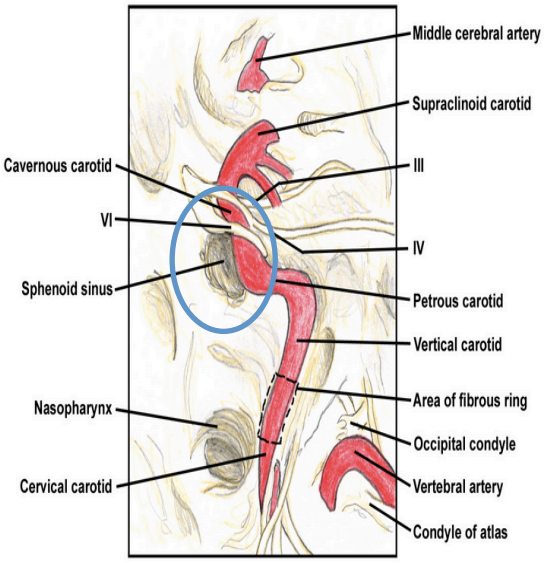

Figure 2: Skull-base Anatomy: The carotid artery lies next to the sphenoid sinus. Image source: http://emedicine.medscape.com/article/882627-overview

1.1.2 Photo-Acoustic Imaging

Photo-acoustic imaging refers to imaging that makes use of the photo-acoustic effect. When a pulsed laser excitation is emitted into the tissue, usually of infrared or radio wavelength, some of the energy is converted into heat. This causes

thermoelastic expansion of the tissue, which results in the emission of ultrasound. Images are generated when transducer probes detect the ultrasound waves. Different properties result in unique absorption of certain wavelengths in different tissues. Thus, optical contrast arises from varying absorption spectra of different tissue. This would allow us to identify bone and the carotid artery in the system that we are developing. In 2008, Wang et al. showed that PAI can be used to non-invasively image infant skulls. Specifically, they showed that their PAI system could be used to detect a simulated vessel placed in a skull phantom.

1.1.3 Xia et al's Computer-Aided Skull-Base Surgery System

In 2008, Dr. Kazanzides' lab developed a system that integrated computer planning and navigation, and robotic assistance for use in skull base surgeries (Xia et al., 2008). The system featured the StealthStation ® navigation system, a NeuroMate ® robotic arm, as well as visualization software 3D Slicer. It allowed for cooperative control and enforced safety constraints through virtual fixtures, which were defined pre-operatively on CT scans. The system exhibited high ergonomic benefits, reducing surgeon stress and fatigue.

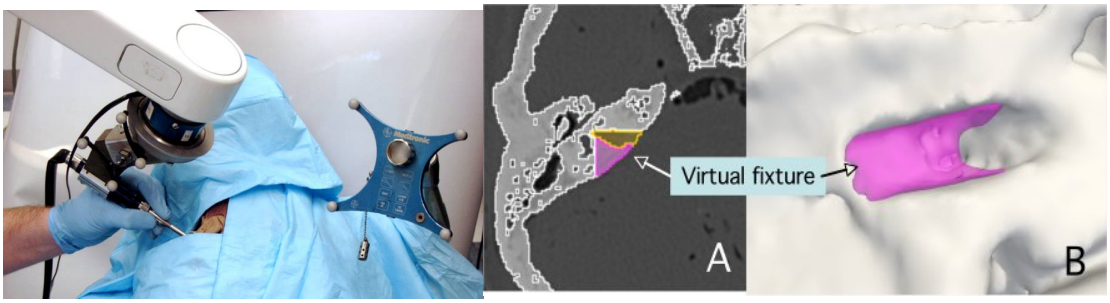

Figure 3: Integrated system for planning, navigation and robotic assistance for skull base surgery by Xia et al. The system enforces safety constraints through virtual fixtures. Image source: Xia, T., Baird, C., Jallo, G., Hayes, K., Nakajima, N., Hata, N. and Kazanzides, P. (2008), An integrated system for planning, navigation and robotic assistance for skull base surgery. Int. J. Med. Robotics Comput. Assist. Surg., 4: 321–330. doi: 10.1002/rcs.213

While this system was developed for a different approach, it is easy adaptable to the transsphenoidal one. However, experiments showed that the system was able to

achieve an average accuracy of 1-2mm, with a maximum error of 3mm. To achieve clinically acceptable errors of the 1mm range, Dr. Kazanzides proposed using intra-operative photo-acoustic imaging (PAI) to reduce uncertainty in the registration. We hypothesize that the use of a computer-integrated skull base surgery system with the integration of intraoperative ultrasound imaging/sensing will provide increased accuracy and therefore improve the feasibility and safety of this method.

2 Goals

2.1 Goals for this project

Our overall goal is to improve the accuracy of computer-aided transphenoidal skull base surgery through the use of intra-operative imaging so as to protect critical structures such as the carotid artery during dangerous processes such as drilling.

Specifically, the goal for this project is to put together and test a basic framework to investigate if the proposed system will reduce the error to clinical specifications. Since our primary concern is in system set-up and registration software development so as to provide proof-of-concept, we will be simulating the intraoperative imaging part of the system.

2.2 Assumptions/Limitations

In simulating the photo-acoustic signal, we will be making the following assumptions: Firstly, we assume that the photo-acoustic signal in reality will be strong enough that it can be detected through the thinnest part of the skull. Secondly, we assume that the intensity of the laser needed to generate this signal is within safety guidelines. Finally, we assume that the equipment needed for the incorporation of PAI into the procedure, such as the endoscopic laser that can be attached to the drill, as well as the ultrasound probe, are already available. Previous

studies suggest that these assumptions are reasonable ones to make. However, validating them in a clinical setting is not within the scope of this project.

3. Materials and Methods

3.1 Technical Approach

Our system is an extension of the one developed in 2008 by Xia et al. Xia et al's original system makes use of a preoperative CT image and navigation system, but not any interoperative imaging. The registration from the CT coordinates to the coordinates of the navigation system is first found using fiducials that are set up before the CT scan. Touching the fiducials with a tracked pointer in the navigation system then gives a set of points corresponding to the segmented fiducials in CT space that allow for a registration between the image and the navigation system. The surgeon then defines a virtual fixture in the CT coordinates, which is transformed to the navigation system through the registration. This sets the boundaries for the surgical drill, preventing it from going outside of a target zone. The intraoperative virtual fixture volume can be reduced to account for the estimated error of the registration. However, as previously remarked, this system presents an inaccuracy higher than standard accepted clinical values of 1mm.

In our new system, a non-invasive imaging method photo-acoustic imaging is used to give feedback as to where the critical structures are in relation to the navigation system during the surgery. This new system would require a pulsed laser attached to the surgical drill, as well as an ultrasound probe. When the laser is activated, photoacoustic waves are detected by the probe that is placed at one of the temples of the forehead. The image obtained as well as the tracked locations of the probe and laser will allow for the derivation of the positional informtion of anatomical features base that can then be registered to the same points on the pre-operative CT image. The position and shape of the virtual fixture can then be altered to avoid critical structures during the procedure.

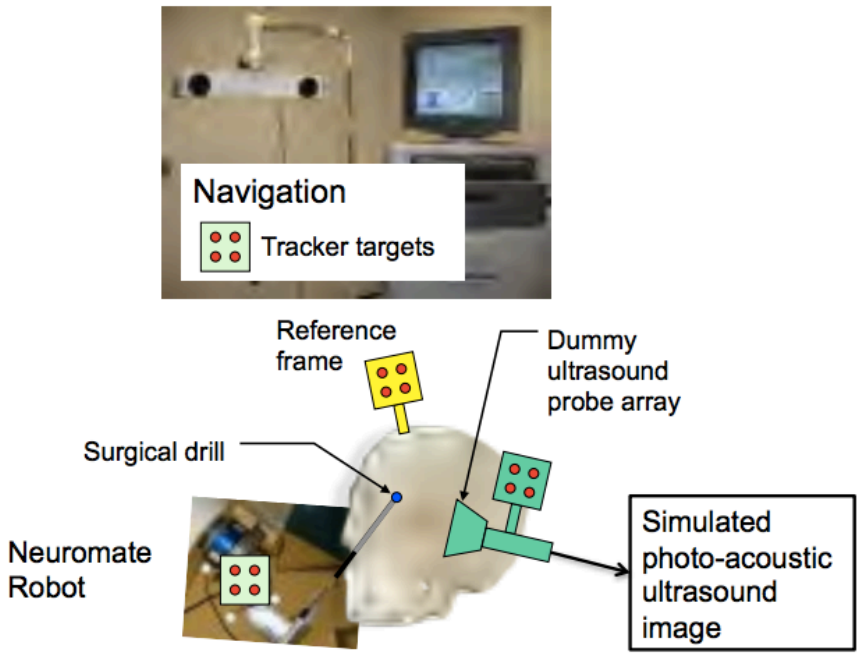

Figure 4: Diagram illustrating system set-up with integration of Stealthstation navigation system, Neuromate robotic arm, and PAI simulation. Image credit: Dr. Kazanzides

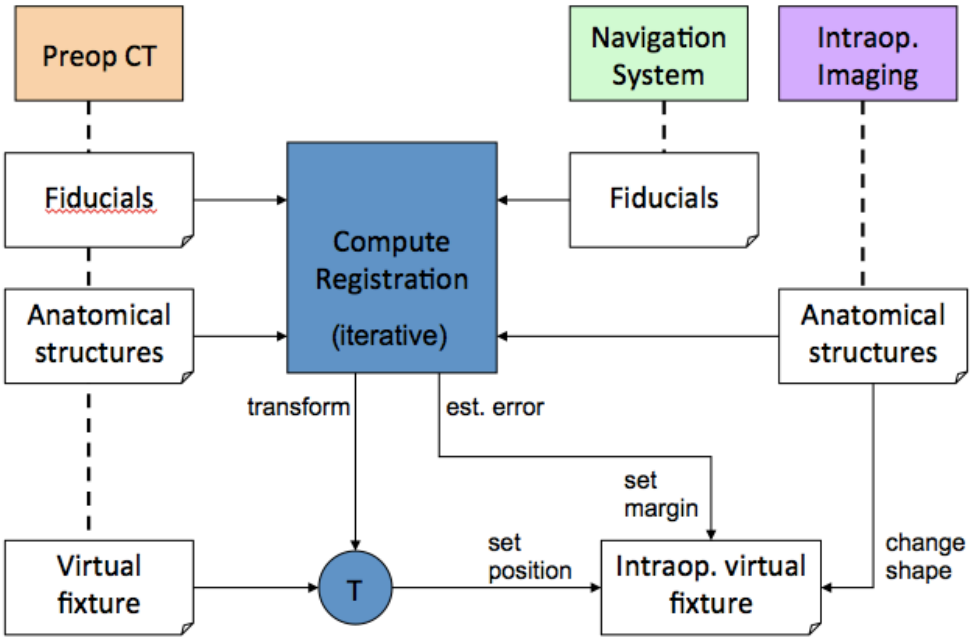

Figure 5: Block diagram illustrating our technical approach. Intraoperative imaging is incorporated into existing system to obtain information during the operation of anatomical structures. The information can then be used to iteratively recompute the registration to the same segmented anatomical features in the pre op CT. Picture credit: Dr. Kazanzides

3.2 Component-Based Software Framework Design

3.2.1 MainTask

Our software makes use of the cisstMultiTask library from the Surgical Assistant Workstation (SAW) library to implement a component-based framework. The MainTask component is derived from mtsTaskPeriodic and defines required interfaces that rely on the sawMedtronicStealthlink component and the sawKeyboard component. The MainTask implements the main program flow, which is divided into two modes: Pre-Operating Mode, and Operating Mode. During Pre-Operating Mode, fiducial points are collected and pre-operative registration is performed. During Operating Mode, photo-acoustic ultrasound is simulated and the points collected are used for the ICP and resulting re-registration. (See Section 2.4)

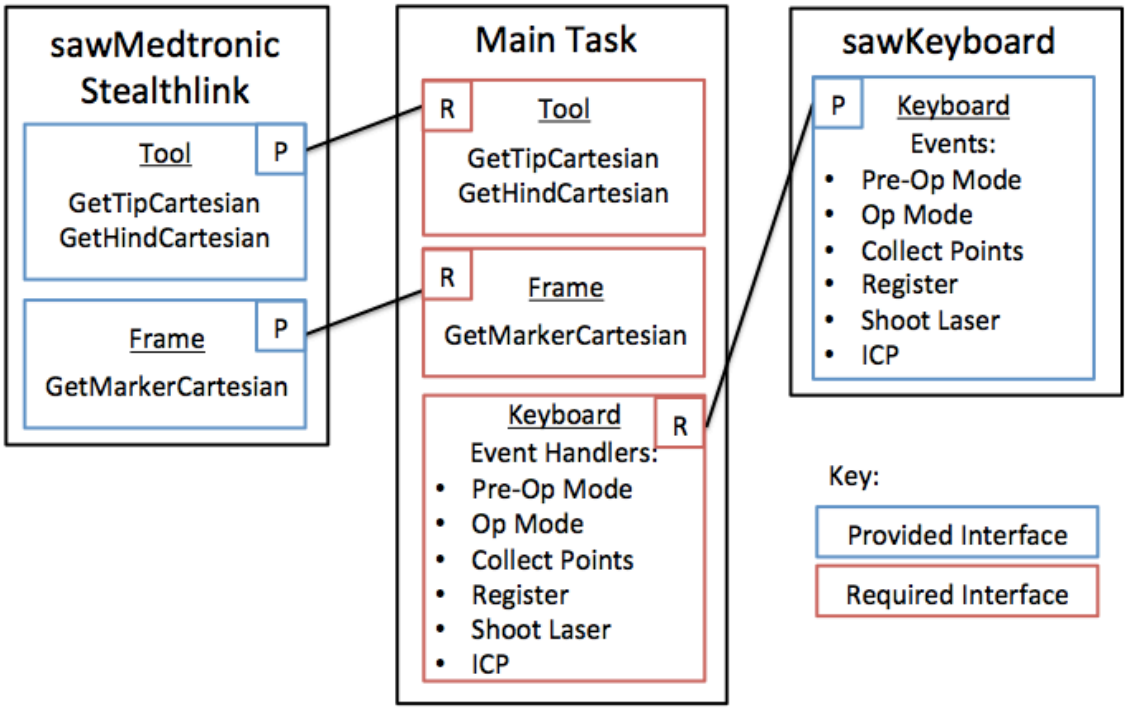

Figure 6: Illustration of the component-based design. A main task derived from mtsTaskPeriodic defines required interfaces that connect to the provided interfaces defined by the sawMedtronicStealthlink and sawKeyboard components.

3.2.2 sawMedtronic Stealthlink

The sawMedtronicStealthlink component interfaces with the Stealthlink research interface. Of relevance to our project is the sawMedtronicStealthlink's provided interface for tools. This provided interface contains read commands for finding the rotation and translation of the pre-defined tip as well as marker frame of those tools that are being tracked by the StealthStation. These tools must be defined in an xml file that is parsed during run-time. The positional information of the tip and marker frame of these tools is given in the StealthStation camera's coordinate system.

However, to be able to find the orientation of the tool, the hind information of the tool is also needed. Since this read command was not already available, the provided interface defined in the code from the sawMedtronicStealthlink library, mtsMedtronicStealthlink.cpp, was modified to also keep track of the hind of the tool as a new entry in its state table. A read command and its corresponding method were then created to get the information of the hind (if defined) of each tool in StealthStation camera coordinates. The hind of each tool in StealthStation camera coordinates is given by $F_t \cdot F_{hind}$. (See figure 10)

3.2.3 sawKeyboard

The sawKeyboard component provides an interface to the keyboard and generates commands and events based on key presses. In our design, the sawKeyboard component is used to provide a user interface with which the user may interact with the MainTask component in real time. The following keyboard commands/events are available:

p	Pre-Operating Mode. The program starts in Pre-Operating mode. When selected again, the points collected for registration and the registration performed during the previous pre-operative segment are reset.

f	Collect fiducial point. This command/event is only available in Pre-Operating Mode. Fiducial points should be collected in a certain pre-defined order.
r	Perform registration using fiducial points collected. This command/event is only available in Pre-Operating Mode and if the expected number of fiducial points (6) is available.
o	Operating mode. The program can only enter Operating mode after a successful pre-operative registration.
s	Shoot laser. The program simulates a laser being shot.
c	Correct registration. The program attempts to correct the registration based on the points that were collected intra-operatively.

3.3 Phantom and Physical Set-Up

3.3.1 Phantom

The final phantom was constructed out of two wooden planks glued together in an L-shaped configuration. Wood was used because our previous choice of cardboard was not rigid enough and would have introduced an additional source of error into our experiments. On one of the faces, a rubber tubing bent in an S-shaped configuration was taped in place and used to represent the carotid artery. 6 plastic screws served as fiducials. Rubber tubing and plastic screws were used in place of our previous choices of metal wires and metal screws, because these resulted in CT artifact. The phantom was built with help from Tutken Sen.

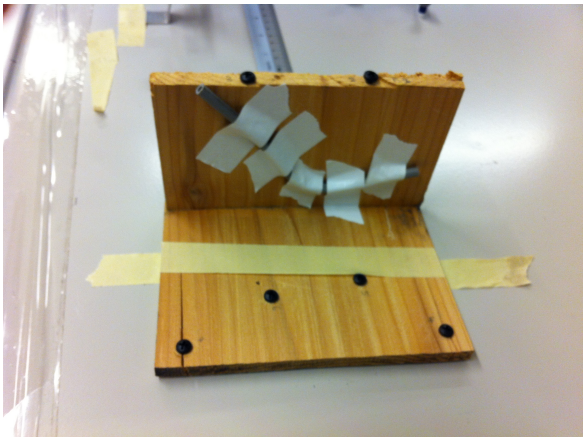

Figure 7: Photograph of the final phantom. The phantom was built out of wood and plastic tubing, with plastic screws serving as fiducials.

A CT scan for the phantom was acquired using Elekta Infinity with the help of Nathan Cho and Esteban Velarde. The resulting DICOM image was loaded into 3D Slicer. Segmentation of the artery was carried out in 3D Slicer using simple thresholding and the data was output in VTK polydata format. The fiducials were annotated manually and saved as cartesian coordinates in a text file.

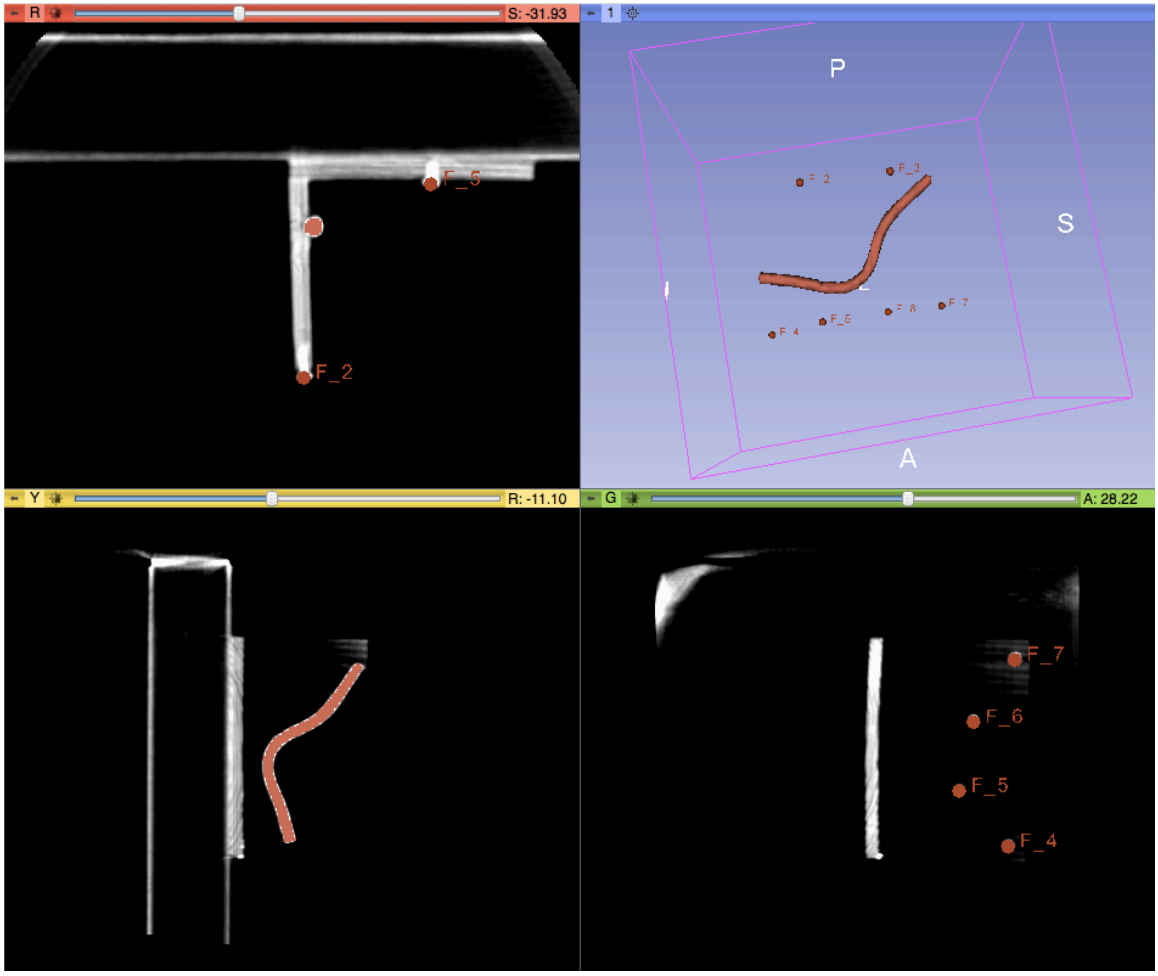

Figure 8: Segmentation of artery and annotation of fiducials in 3D Slicer. A simple thresholding method was used to segment the artery, as can be seen in the bottom-right window. The fiducials were annotated as F_# using the annotation tool, as can be depicted in the top-left and bottom-right window. The resulting segmentation and annotations are depicted in the top-left window.

3.3.2 Physical Set-Up

The StealthStation is a surgical navigation optical tracking system. With its camera, it is able to determine the frames of certain rigid bodies using reflection beads

arranged in specific patterns. The tool that we used has its own frame and a defined translation to the tip and hind of the tool. We use it in place of Using the tip and hind information, we were able to generate a line, which simulates the path of a laser. These points were used in reference to the frame coordinate system rather than the camera coordinate system. This way, if the camera is accidently moved, since the tool and phantom would still have the same relative positions to the reference frame, there will be a negligible affect. Furthermore, this better simulates surgical conditions as a rigid frame would most likely be attached to the surgical setup to act as the reference frame.

The phantom and reference frame were placed next to each other within view of the StealthStation camera and fixed to the "operating" table. The tool was freely moved around to act as a simulated laser whose position is also being tracked by the StealthStation.

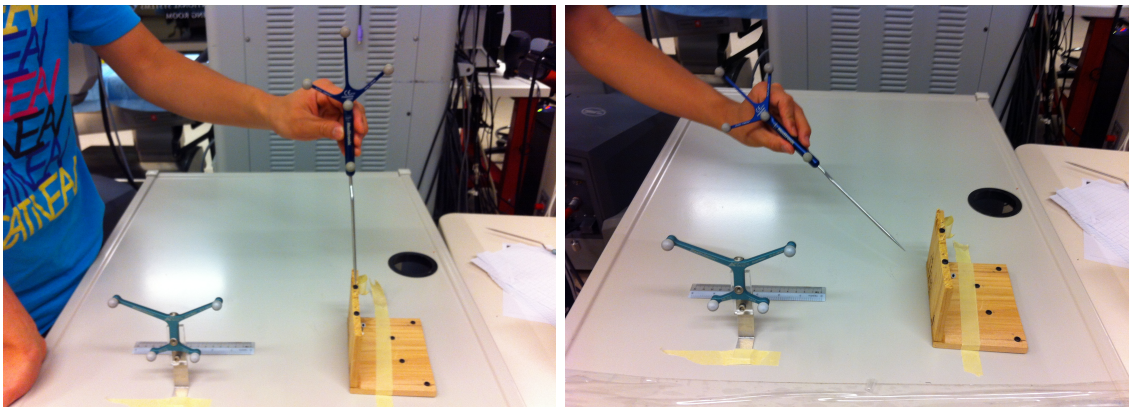

Figure 9: Set-up with frame (green), tool (blue) and the phantom. In the picture on the left, the tip of the tool is used to touch the first plastic screw. Th points collected will be used for registration. In the picture on the right, the tool stands in for the laser. The tip and hind of the tool is used to calculate if the laser intersects with the artery on the other side of the wooden plank.

3.4 Software Implementation and Program Flow

3.4.1 Initialization

The annotated fiducials and segmented artery in 3D slicer coordinates are first parsed and stored in VTK data structures. Other variables such as flags to determine when to collect data and the mode that the current program is in are also initialized.

3.4.2 Pre-Operation

The program starts in Pre-Operating Mode. While in Pre-Operating Mode, each of the fiducial points is touched in the pre-defined order with the tip of the tool and the tip coordinates in the frame coordinate system are computed and stored. The transformation to find the tip coordinate in the coordinate system of the frame is $F_f^{-1}F_tF_{hind}$.

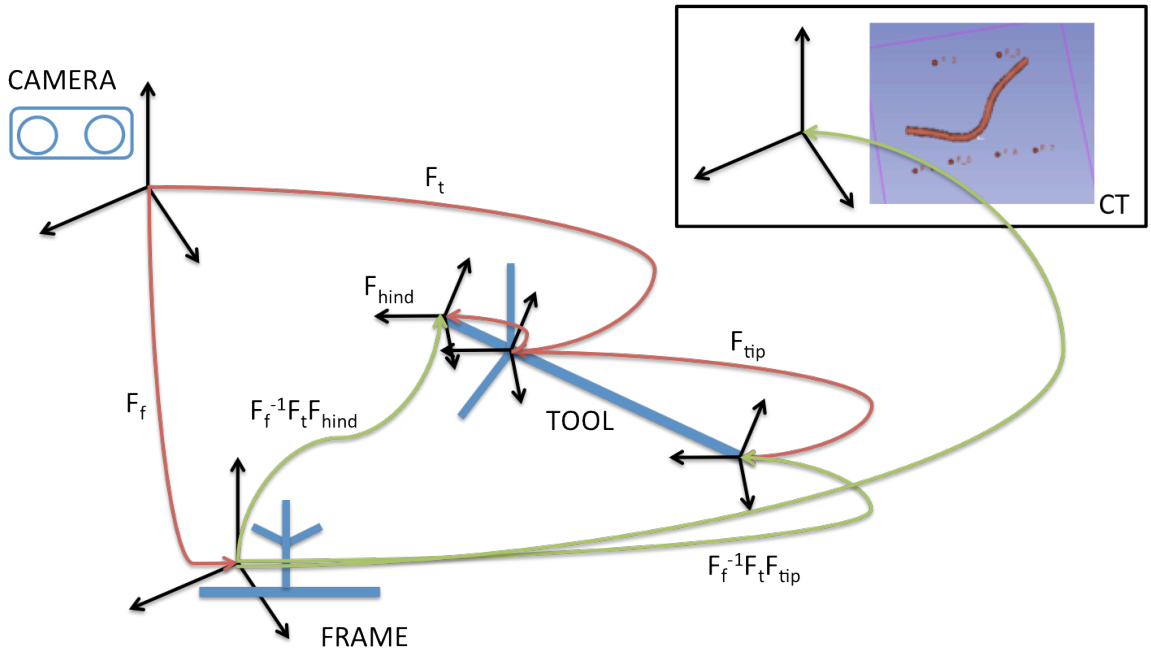

Figure 10: Diagram illustrating the transformations between each coordinate system. The red arrows are those that we know from the StealthStation. The green arrows are those that we must calculate.

After the six points corresponding to the fiducial points are collected, a rigid registration is performed using the VTK library's rigid registration method, vtkLandmarkTransform, with the mode set to VTK_LANDMARK_RIGIDBODY (rotation and translation only). The resulting transformation is applied to the

segmented artery in 3D slicer coordinates to obtain the 'ground-truth' artery in frame coordinates. This segmented artery in frame coordinates is taken to be the ground truth for all further calculations. We assume that this ground truth is close to the actual ground truth because the experiment is being performed in an ideal situation where the rigid phantom does not move.

For testing, some error is introduced by perturbing the fiducial points obtained in the frame coordinates and then finding an error registration using the same method. This error transformation is applied to the segmented artery in 3D slicer coordinates to obtain the 'error' artery in frame coordinates. This 'error' artery represents the artery that one would have obtained under less-than-ideal conditions and will later be used during ICP. (That is, the 'ground truth' artery is not actually known during a normal procedure, and only the 'error' artery is available. However, for the purposes of testing, we have established a ground truth to enable error quantification.)

In general, error is found by comparing two artery surfaces. It is computed as the average of the euclidean distances between each corresponding point on the artery surfaces.

3.4.3 Operating Mode

During Operating mode, we simulate the points collected from photo-acoustic imaging using one of the two methods detailed in 2.2.4. After the points are collected, the ICP algorithm is used to find those points that they correspond to on the surface of the artery. We used the ICP algorithm implemented in the VTK library, vtkIterativeClosestPointTransform, with the vtkLandmarkTransform once again set to VTK_LANDMARK_RIGIDBODY. The ICP was performed with two target surfaces: the 'error' artery surface in frame coordinates as well as the artery surface in CT coordinates. We then compared the results.

If the ICP was successful, a registration is performed to find the rigid transformation between the set of 'error' fiducials in frame coordinates supplemented by simulated photo-acoustic imaging points from the 'ground truth' artery in frame coordinates, and the set of annotated fiducials in CT coordinates supplemented by the corresponding ICP points in CT coordinates as computed in the prevous step.

The new transformation is then applied to the artery surface in CT coordinates to obtain the 'corrected' artery surface in frame coordinates. Error is then calculated between the 'corrected' artery with reference to the 'ground truth' artery and this error is compared to the initial error that was introduced.

3.4.4 Simulation of Photo-Acoustic Imaging

To test our framework, we created simple simulations of photo-acoustic imaging, keeping in mind that using a laser and a stationary single-cell probe as was originally proposed would provide only a single point for each time the laser was fired.

3.4.4.1 Random sampling

Our first simulation did not take into account where the laser was likely to shoot. Instead, the simulation randomly sampled points from the surface of the ground-truth artery. The purpose of this was to investigate variables required for the ICP to succeed.

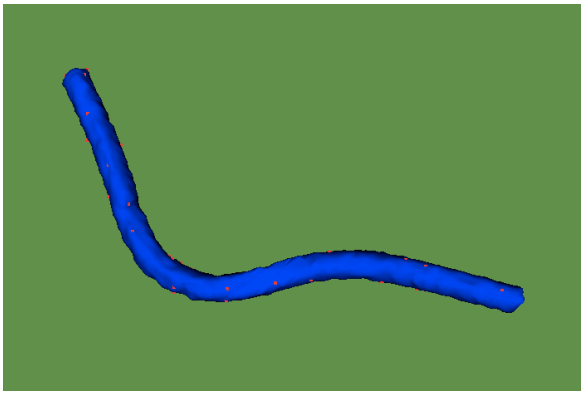

Figure 11: Artery with random points sampled. The points that were sampled are in red.

3.4.4.2 Intersection with artery surface

The second simulation makes use of the hand-held tool being tracked by the StealthStation, standing in for the laser. Using the tracked position of the tool's tip and hind coordinates, the path of the laser was modeled as an extended ray parallel to the tool that extended from the tip of the tool. The intersection of the laser's path with the 'ground truth' artery surface in frame coordinates was then found. To maximize efficiency, the 'ground truth' artery surface was represented as a vtkModifiedBSPTree, which is a binary space partitioning tree that enables fast searches.

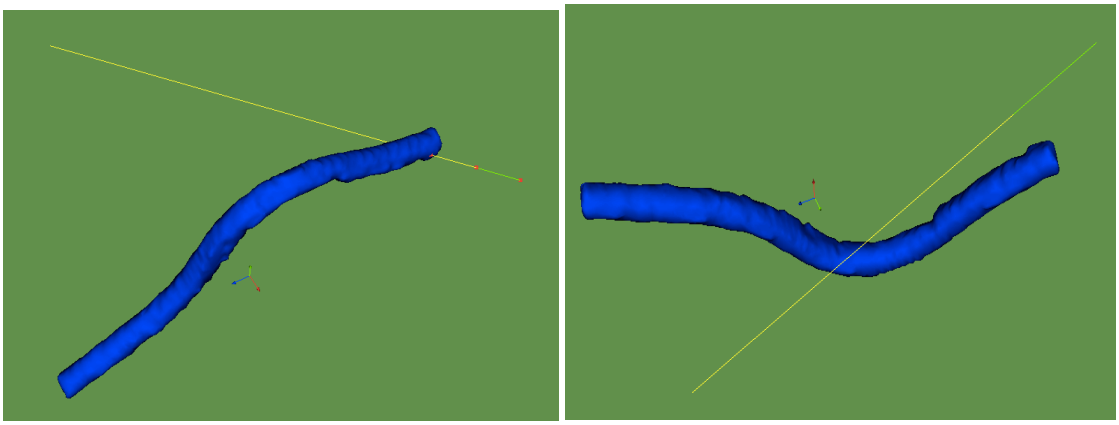

Figure 12: Simulating intersection (left) and no-intersection (right). On the left, the laser (yellow) extending from the tool (blue) intersects with the artery. The red point corresponding to the first point of intersection with the artery on the surface of the artery is collected.

3.4.4.3 Advantages of each type of simulation

The advantage of the first simulation is that it is much faster because it does not require that a person move the tool to collect the points and does not take into account when the tool is not in line with the artery surface. This then allowed us to run hundreds of trial simulations to find reliable estimations of the mean and standard deviations of the 'corrected' errors under different conditions (See Section 3.5)

However, the second simulation is more realistic because a person is wielding the laser and this affects how the points are being collected. A surgeon moving the laser

would not be collecting random points. He or she also does not know where the artery is located and this may affect the spread of points that he or she collects.

3.5 Visualization

At the end of each simulation, for the sake of visualization, the ground-truth artery and fiducials, the error artery and fiducials and the corrected artery and fiducials are rendered in VTK for visualization. The ground-truth artery and fiducials are in blue, the error artery and fiducials are red, and the corrected artery and fiducials are in yellow.

3.6 Summary

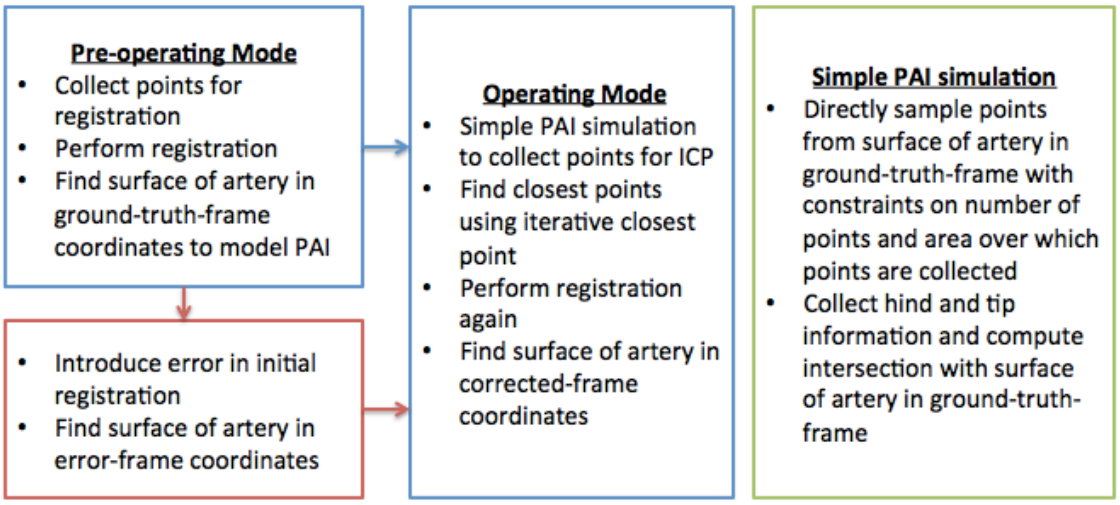

Figure 12: Summary of the program flow. The program starts in the pre-operating mode when points are being collected to perform pre-operative registration. Some error is introduced to simulate less-than-ideal conditions. The program then moves to operating mode to try to correct the error.

3.5 Experiments

We investigated the conditions under which error was successfully reduced to below 1mm. In particular, we were interested in variables such as the number of photo-acoustic imaging points, and the area over which the points were being collected, and how these affected the resulting 'corrected' error.

For the first type of PAI simulation, we varied the number of points between 5 and 35 with the step size of 5. We also varied the area over which the points were allowed to be collected as a function of the radius of the first collected point, from 10mm to 90mm. Finally, we varied the total error introduced, through a combination of translational and rotational error. As mentioned in section 2.2.3, we also compared the final results when the target of the ICP was the artery surface in CT coordinates, and when the target of the ICP was the 'error' artery surface in frame coordinates.

For the second type of PAI simulation, we varied the number of points between 5 and 35, with a step size of 5. However, this time we used the physical phantom and a tracked tool. Also, as we increased the number of points, the previous points were kept instead of having an entirely new sample between 5 and 10 points. This gives us a better idea of whether having more points for ICP reduces the error. Using the tracked tool, we could shoot a simulated laser using tip and hind information. If the line from the hind to the tip intersected the phantom artery, the point of intersection was collected. If there was no intersection, it was marked as a failure. Similar to the previous simulation, we also introduced varying amounts of initial error into the registration with a combination of translational and rotational error.

4 Results

4.1 Results: Proof of Concept

Overall, we were able to demonstrate a reduction of error by incorporating a simple simulated ultrasound system. In our first simulation, where random points were sampled, we were able to reduce an introduced error of **5.1939mm** to **0.6572mm**, **3.2266mm** to **0.4376mm**, and **1.2746mm** to **0.1727mm**. These results were collected under the most ideal conditions for ICP, having the largest amount of space to collect points (90mm) and collecting the most amounts of points (35). In

particular, for the reduction from 3.2266mm, the standard deviation is low, suggesting that corrected errors are reliably lower than the 1mm clinical value. Hence, these results suggest that a system incorporating intra-operative imaging shows potential of the method working, given that these prior conditions are fulfilled. (See Section 4.2 for discussion on variables affecting the final error) From the table below, there is a general trend of higher reduction of error as the area from which the points are collected increases and as more points are collected.

Mean Registration Error After Re-Registration (Simulated), in mm (N = 100)

Initial Error: 5.1939mm		**Number of Points Collected for ICP**						
		5	10	15	20	25	30	35
Collection Area Radius (mm)	10	4.1448	3.5840	3.4946	3.1910	3.2299	3.2596	3.0766
	30	4.0586	3.2087	2.5299	2.2798	2.2798	2.1172	2.1917
	50	3.9582	2.8922	2.2755	1.8479	1.6616	1.5621	1.4855
	70	3.8615	2.5300	2.5300	1.4725	1.2550	0.9885	0.7939
	90	3.7649	2.3008	1.5807	1.1680	0.9154	0.7464	0.6573

Mean Registration Error After Re-Registration (Simulated), in mm (N = 100)

Initial Error: 3.2266mm		**Number of Points Collected for ICP**						
		5	10	15	20	25	30	35
Collection Area Radius (mm)	10	2.5449	2.1113	1.9190	1.8818	1.7226	1.6828	1.6554
	30	2.4875	1.8177	1.5458	1.2937	1.1958	1.0865	0.9253
	50	2.4320	1.6312	1.1934	0.9909	0.8572	0.7838	0.7393
	70	2.2938	1.4288	0.9960	0.8352	0.6546	0.5796	0.5197

	90	2.3439	1.3902	0.9112	0.6971	0.5932	0.4912	0.4376

Mean Registration Error After Re-Registration (Simulated), in mm (N = 100)

Initial Error: 1.2746mm		**Number of Points Collected for ICP**						
		5	10	15	20	25	30	35
Collection Area Radius (mm)	10	0.9243	0.7730	0.6468	0.6273	0.5893	0.6027	0.5307
	30	0.8991	0.6646	0.5290	0.4515	0.3861	0.3527	0.3351
	50	0.9593	0.5976	0.4419	0.3608	0.3335	0.2717	0.2576
	70	0.8996	0.5235	0.3780	0.3065	0.2552	0.2238	0.1991
	90	0.8379	0.4904	0.3488	0.2727	0.2260	0.1943	0.1727

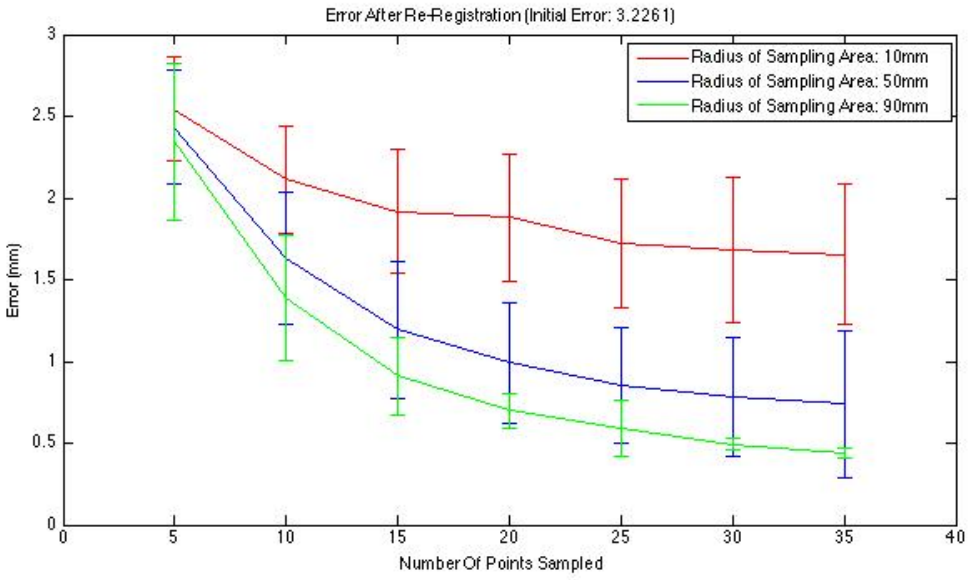

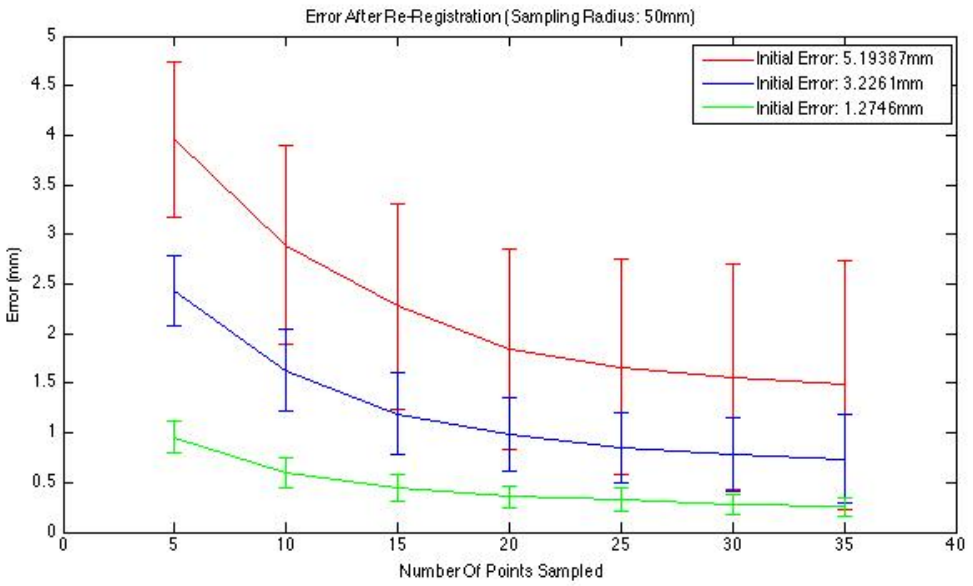

Figure 14: Plots using random sampling with varying radius of sampling area (top) and varying initial errors (top). The error bars mark the standard deviation from the mean. In both plots the greater the number of points sampled, the lower the error. Note that an initial error of 3.2261 was successfully reduced to below 1mm with extremely low standard deviation (error bars < 1mm).

However, even with a smaller collection size and area, there is still the potential for reducing error to under the clinical threshold of about 1mm, depending on the initial error. Another thing to notice is that 5 points for ICP is not sufficient in significantly reducing error. The greatest increase in the reduction of error occurs between 5 and 10 points, suggesting that in clinical settings, we would want to pursue at least this many points for ICP. Furthermore, the collection area does not play a large role in reducing error before 10 points collected. Similarly, the greatest increase in the reduction of error occurs between 10mm and 30mm of area.

These results are further supported by our experiments with a physical model of an artery. In the example pictured below, an introduced error of 5.37103mm was reduced to 0.674765mm with 40 points collected over the artery's entire surface. Blue corresponds to ground truth, red corresponds to error, and yellow corresponds to the result after correction.

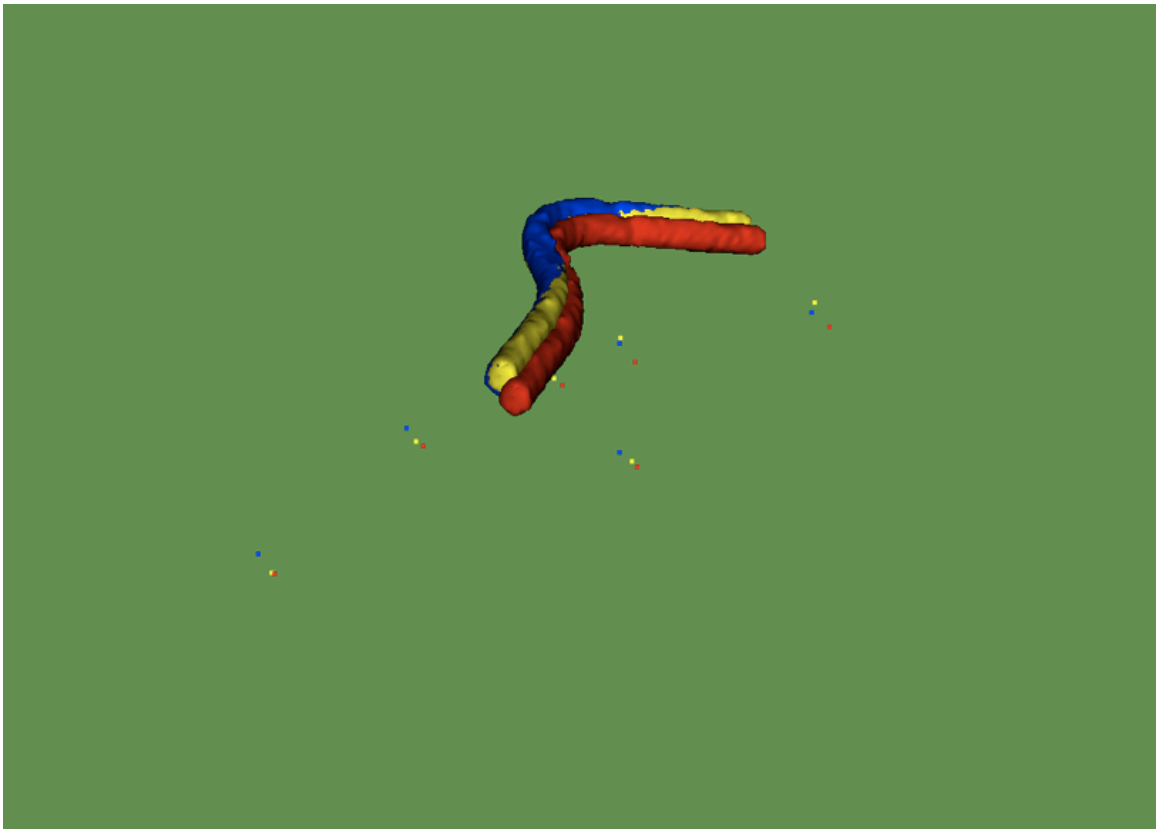

Figure 15: Example of an error reduction from 5.37103 mm to 0.674765 mm with 40 points collected with the 'laser' over the entire surface of the artery. Blue corresponds to ground truth, red corresponds to error, and yellow corresponds to the result following correction.

Using the StealthStation tracked probe, we were able to simulate an ultrasound laser. We were able to reduce an initial error of **5.2912mm** to **0.9837mm**, **3.0173mm** to **0.5706mm**, and **1.0292mm** to **0.2223mm**. Similar patterns in the data were noticed in these trials versus the completely computer simulated experiments.

Mean Registration Error After Re-Registration (Phantom), in mm (N = 5)

Initial Error: 4.96881mm		**Number of Points Collected for ICP**						
		5	10	15	20	25	30	35
Collection	10	4.8888	4.5776	4.5369	4.6027	4.4031	4.4741	4.4936

Area Radius (mm)	30	4.9787	4.5693	4.6634	4.4660	4.3374	4.2662	4.0251
	50	4.5928	3.8372	3.5778	2.5162	2.2270	1.2443	1.0560
	90	4.3814	3.4905	3.4108	1.4513	1.3977	1.0316	0.9837

Mean Registration Error After Re-Registration (Phantom), in mm (N = 5)

Initial Error: 2.89402mm		**Number of Points Collected for ICP**						
		5	10	15	20	25	30	35
Collection Area Radius (mm)	10	2.7133	2.2998	2.1146	1.8020	1.6786	1.5745	1.4988
	30	2.6015	2.2088	1.7287	1.5812	1.4011	1.3123	1.2736
	50	2.5362	1.6733	1.2659	1.0580	0.8871	0.7599	0.7043
	90	2.6889	1.7686	1.2073	0.8712	0.7726	0.6640	0.5706

Mean Registration Error After Re-Registration (Phantom), in mm (N = 5)

Initial Error: 1.01808mm		**Number of Points Collected for ICP**						
		5	10	15	20	25	30	35
Collection Area Radius (mm)	10	0.8651	0.6855	0.6819	0.6389	0.5947	0.5923	0.5662
	30	0.7900	0.6488	0.5979	0.5689	0.5043	0.4893	0.4429
	50	0.7271	0.6018	0.4304	0.3263	0.3093	0.2930	0.2711
	90	0.7275	0.6827	0.4249	0.3137	0.2641	0.2633	0.2223

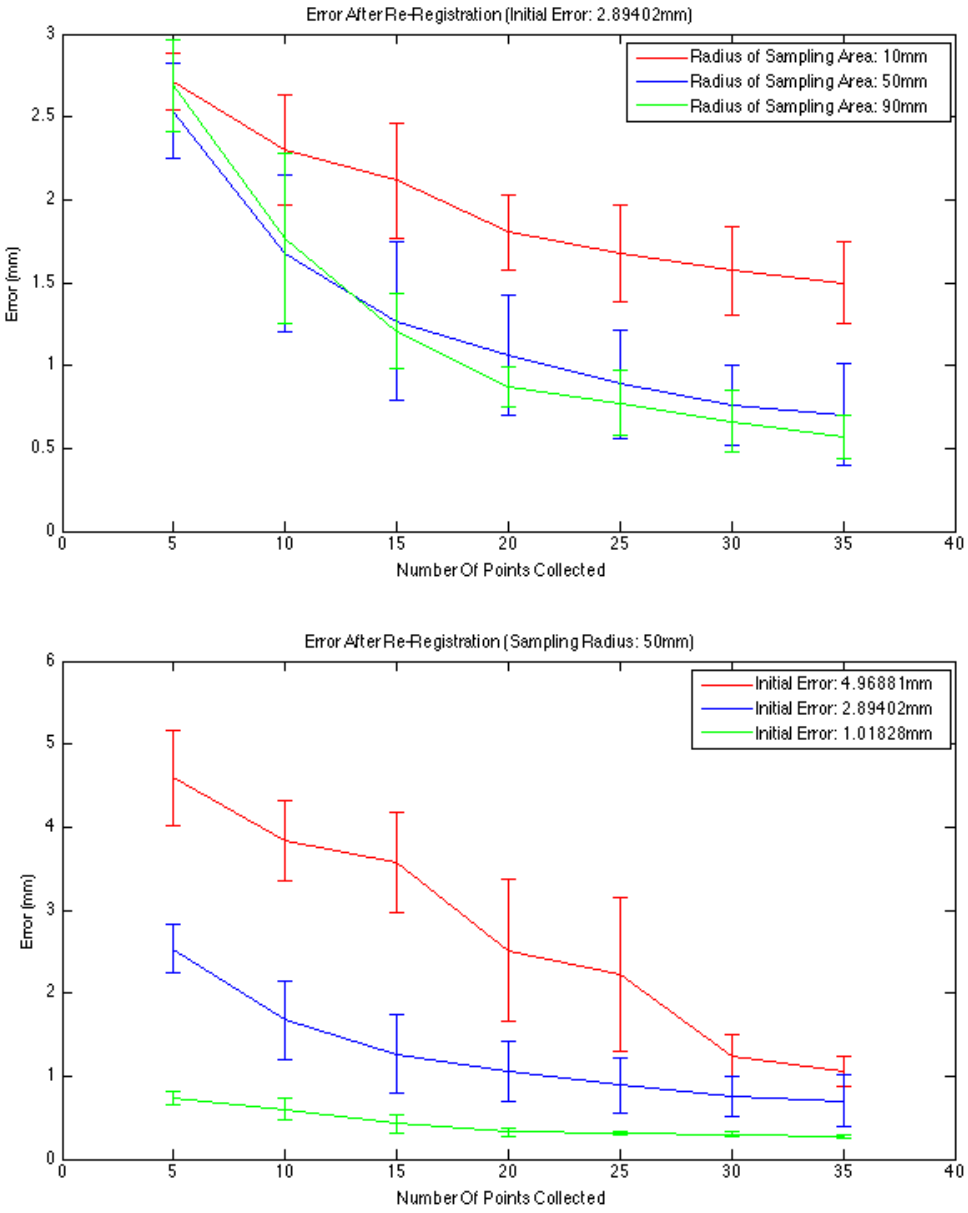

Figure 16: Plots using collection with varying radius of sampling area (top) and varying initial errors (top). The error bars mark the standard deviation from the mean. In both plots the greater the number of points sampled, the lower the error. Under ideal conditions error is once again reduced below 1mm.

One particularly interesting phenomena is that there was no error reduction with a high initial error (~5.0mm) when the area was small (< 50mm radius) independent how many points were sampled. This may be due to the fact that ICP may be relatively useless in correcting large amounts of error when the given information is

small. Luckily, we are only expected errors of around 3mm maximum with the current system as published by Kazanzides et al.

There was a relatively high standard deviation (>1mm) for non-ideal conditions. Futhermore, from the raw data, we can see there would be really good re-registrations from the ICP, but there would also be relatively bad re-registrations from the ICP. This likely caused the result in a relatively high standard deviation for the experiments that started with a high initial introduced error. The standard deviation reflects the consistency of the ICP in the registration. When the initial error is higher, there is less consistency in the ICP due to the fact that there is a greater range for error correction. Thus, there will be very good error corrections and very bad error corrections. However, for trials will low initial error, the standard deviation is significantly lower, signifying the increased consistency of this procedure. We propose that in an improved version of our system, re-correction is done iteratively instead of just once to guarantee that the final error meets clinical specifications.

4.2 Results: Variables affecting reduction of error

4.2.1 Sampling Variables

From the results, we can see that there are two main factors that affect accuracy of the system: **(1)** the number of points used for ICP and **(2)** the area from which points are collected.

Obviously, as the number of points used for ICP increases, we have more information about the ground-truth surface of the artery and the transformation to the introduced error artery can be more accurate. However, there were individual cases where adding more ICP points resulting in a lower accuracy. The general trend across multiple trials yielded a dominant trend in increasing accuracy with increasing number of points. If even more points were included, the error would be

very low, but it may be difficult in clinical procedure to acquire that much information.

The second trend accounts for spacing between points. If all of the points we sample are clumped together, it would be difficult to use ICP to find the transformation to the surface model of the artery because the clump could correspond to a variety of orientations and positions on the artery. However, if points are sampled all across the artery, this will help map the shape of the artery, resulting in an increased accuracy of the transformation following ICP. Once again, in a clinical setting, it would be beneficial to have some sort of laser with a relatively large range of motion, which would allow us to sample points within a wide radius.

4.2.2 Laser

For the most part, the results with the physical model and laser simulation were relatively similar to the purely computation simulation. The error reduction was slightly less. This is because in shooting the laser, we are only gathering points on one side of the artery (we cannot shoot a laser 360 degrees around the artery during surgery), whereas in random sampling previously, there was the potential to sample points on opposite sides of the artery. Surprisingly, this did not decrease the magnitude of error reduction significantly. The only other noticeable difference was the inability for the system to correct for around 5mm of error within a 10mm or 30mm sampling radius, despite a higher number of points (up to 35) as mentioned previously (see 4.1).

5 Discussion and Conclusions

In this study, an ultrasound imaging system was tested to examine the successes and drawback in using intraoperative imaging to correct for errors in currently existing systems for computer-integrated skull base surgeries. The designed software implementation of this simulation created a framework for integration of

PAI and tested the accuracies of such a system. The purpose of the study was to act as a proof-of-concept before proceeding with increased effort into such a system. Based on these results, there seems to be a relatively high potential for this framework to be incorporated into previously existing systems for eventual testing. As such, there is still much more work to be done.

Although we demonstrated a potential method of using PAI to increase accuracy during skull base surgery, there are still many considerations that must be tested. The greatest error reduction occurred when there were many points collected for ICP and the area for collection of these points were large. However, under surgical settings, these ideals conditions will not be present. It takes time to collect points. We must consider how to collect a considerable amount of points in a limited range of movement, similar to how much spatial freedom a surgeon may have. There is potential in using 2D ultrasound scanning, instead of the 1D simulation that we demonstrated. This will allow for the collection of much more data over a shorter period of time. Rapid pulsing of the laser during the surgery can provide constant information as the surgeon moves the tool around. Many of these solutions require a more clinical implementation of our framework, which is where future direction should be focused.

Futhermore, the geometry of the points tends to have an effect on the accuracy of the system. Even if there are a high number of points, it is more efficient if these points are spaced out across the artery, as demonstrated by the increased accuracy as area of collection was increased. Specific spatial arrangements of these points must be tested to determine which increase the accuracy the most. In a clinical setting, a laser system could be developed to fire in a specific pattern to take advantage of this phenomenon. These considerations should also be examined.

Finally, as previously remarked, one thing that can be done to improve the system is to perform ICP and the re-correction iteratively, instead of just once. This would

likely reduce the standard deviation of the final corrected error, therefore guaranteeing error reduction to below clinical threshold.

6 Management Summary

6.1 Summary

The delays to our schedule were largely due to phantom design. As a result of that, we could not debug our software. We had also shifted the focus of our project to concentrate on testing whether the ICP could reduce the error from our initial proposed focus, which was on simulating the ICP itself. The reason for this was because our proposed method of simulations, k-wave, proved to be too computationally intensive for use with the rest of our software framework. This resulted in modifications in our expected deliverables and dependencies (as presented during our checkpoint presentations). All dependencies that we required for our expected deliverables were eventually resolved. We met with our mentor Dr. Kazanzides once a week for feedback on our project.

6.2 Credits

The project was divided into three main portions, consisting of phantom design and construction, software framework development and implementation, and experimental design and data collection. Phantom design and construction was handled by Allen Zhu, with help from Tutken Sen and Nathan Cho. Software design and implementation was handled by Grace Yeo, with some preliminary help from Anton Deguet. Both Allen Zhu and Grace Yeo contributed to experimentation, data collection, and analysis. Furthermore, ultrasound expertise was sought from Dr. Muyinatu Bell and general guidance and support came from Dr. Peter Kazanzides throughout the process.

		Feb			March				April				May		
		1	2	3	1	2	3	4	1	2	3	4	1	2	3
PHASE 1: PLANNING AND BACKGROUND															
Literature Review	✔														
Project Planning	✔														
Photoacoustic Imaging Tutorial	✔														
K-wave Tutorial	✔														
PHASE 2: DESIGN, SET-UP, SIMULATIONS															
Experimental Design	✔														
Phantom Design	✔														
Experimental Set-Up	✔														
Build Phantom/CT Scan of Phantom	✔														
K-wave Simulations															
Registration Software Design **(March 31)**	✔														
PHASE 3: SOFTWARE, EXPERIMENTATION, DATA ANALYSIS															
Registration Software Implementation	✔														
Registration Software Debugging	✔														
Experiments on Simple Phantom (I)	✔														
Data Analysis (I) **(April 4 → May 3)**	✔														
PHASE 4: EXTENSION, FINAL REPORT AND PRESENTATION															
Integration of Neuromate															
Experimental Set-Up															
Experiments on Simple Phantom (II)															
Data Analysis (II)															
Visualization in VTK	✔														
Final Report	✔														
Final Presentation **(May 13)**	✔														
Documentation	✔														

Figure 17: Final Project Timeline. Red boxes mark delays and were mostly as a result of the propogation of the initial delay in building our phantom.

6.3 Deliverables

We met all of our modified minimum and expected deliverables, and had begun process on our maximum deliverable.

Delivered:

- Simulation of photo-acoustic imaging based on tracked location of hand-held tool with respect to anatomy
- Software framework for incorporation of a photo-acoustic imaging with other computer-integrated surgical systems
- Experimental framework to test accuracy of such a system
- Demonstration of error reduction using this system
- Simple phantom of human carotid artery
- Experimental data regarding optimal conditions for using ICP with photo-acoustic imaging
- Implementation of pre-operative registration
- Implementation of re-registration following simulated intraoperative imaging
- **Proof of concept:** demonstrate this system can recover the correct registration despite error

To be delivered:

- Visualization of system using 3D Slicer or VTK

6.4 Future Direction

As previously discussed, future work and studies should aim to address the following:

- Design and implementation of GUI interface and real-time visualization
- Incorporation of Neuromate system and virtual fixtures implementations
- Incorporation of actual PAI system

- Test usage of 2D ultrasound imaging to increase accuracy
- Testing spatial arrangement of points on the surface of artery to increase accuracy of ICP procedure
- Experiments on cadaver skulls and obtain surgeon feedback
- Determine potential for better optimization of ICP protocol specific to this system (instead of just using the VTK implementation) or using multiple iterations of ICP to correct the error (for e.g., re-running ICP with every new point collected)

6.5 Lessons Learned

- Intraoperative imaging has high potential in reducing initial, pre-operative registration errors for increased accuracy in skull base surgeries
- Extend of error reduction is dependent on number of points collection and area of collection
- ICP must be optimized in clinical settings for implementation of this system
- 1D photo-acoustic imaging may not be sufficient in a clinical setting
- Prospects of using a 2D probe should be explored

7 References

- Xia, T., Baird, C., Jallo, G., Hayes, K., Nakajima, N., Hata, N. and Kazanzides, P. (2008), An integrated system for planning, navigation and robotic assistance for skull base surgery. Int. J. Med. Robotics Comput. Assist. Surg., 4: 321–330. doi: 10.1002/rcs.213
- JF Frazier, K Chaichana, GI Jallo, A Quiñones-Hinojosa, “Combined endoscopic and microscopic management of pediatric pituitary region tumors through one nostril: technical note with case illustrations”, *Childs Nervous System*, Vol 24, pp 1469–1478, 2008

- Cappabianca P, Cavallo LM, Colao A, et al. Surgical complications associated with the endoscopic endonasal transsphenoidal approach for pituitary adenomas. J Neurosurg 2002;97:293–8.
- Xueding Wang, David L. Chamberland, Guohua Xi, Noninvasive reflection mode photoacoustic imaging through infant skull toward imaging of neonatal brains, Journal of Neuroscience Methods, Volume 168, Issue 2, 15 March 2008, Pages 412-421, ISSN 0165-0270, 10.1016/j.jneumeth.2007.11.007
- B. E. Treeby and B. T. Cox, "k-Wave: MATLAB toolbox for the simulation and reconstruction of photoacoustic wave-fields," J. Biomed. Opt., vol. 15, no. 2, p. 021314, 2010
- Kolkman, R., Steenbergen, W., and van Leeuwen, T., “In vivo photoacoustic imaging of blood vessels with a pulsed laser diode,” Lasers in medical science 21(3), 134–139 (2006).

8 Appendices

cs446_grp10_final.tar.gz contains code for (1) modifications to the sawMedtronicStealthlink provided interfaces, (2) sampling simulation, (3) framework with laser simulation, (4) raw data: artery segmentation and fiducial annotations. See README in the code submission folder.